

Considering a long reference scale in photogrammetric bundle adjustment for evaluating gravity-induced focal length variation of a VGOS radio

Downloaded from: https://research.chalmers.se, 2026-11-23 02:10 UTC

Citation for the original published paper (version of record):
Lösler, M., Kopitzke, K., Eschelbach, C. et al (2026). Considering a long reference scale in photogrammetric bundle adjustment for evaluating
gravity-induced focal length variation of a VGOS radio telescope. Measurement Science and Technology, 37(42). http://dx.doi.org/10.1088/1361-6501/aeaf0c

N.B. When citing this work, cite the original published paper.

research.chalmers.se offers the possibility of retrieving research publications produced at Chalmers University of Technology. It covers all kind of research output: articles, dissertations, conference papers, reports etc. since 2004. research.chalmers.se is administrated and maintained by Chalmers Library

(article starts on next page)

Measurement Science
and Technology

PURPOSE-LED
PUBLISHING™

PAPER • **OPEN ACCESS**

Considering a long reference scale in photogrammetric bundle adjustment for evaluating gravity-induced focal length variation of a VGOS radio telescope

To cite this article: Michael Lösler *et al* 2026 *Meas. Sci. Technol.* **37** 425002

View the article online for updates and enhancements.

You may also like

- An experimental verification of the compensation of length change of line scales caused by ambient air pressure
Akira Takahashi and Nobuharu Miwa
- On-orbit calibration of multi-view photogrammetry system for satellite antenna measurement
Xinming Li, Lianglei Xiong, Yibo Yan et al.
- Research on accuracy testing of close-range photogrammetry for geometric feature measurement in particle accelerator
Enchen Wu, Xiao Li, Xiaolong Wang et al.

4-CHANNEL CONFIGURABLE
OPEN RF ENGINE FOR
QUANTUM EXPERIMENTS

LUGUS
Developed by Instrumentation Technologies

High bandwith arbitraty waveform generator (AWG)
Up to 1.25 GSPS

Open & programmable
Full access to FPGA implementation and firmware

Compatible with control frameworks
LabScript, ARTIQ, etc.

High power outputs
Up to 36 dBm

High-bandwidth feedback control
Open or closed-loop operation,
Feedback bandwidth up to 125 MSPS

This content was downloaded from IP address 155.4.17.34 on 26/10/2026 at 05:36

Measurement Science and Technology

Check for updates

OPEN ACCESS

RECEIVED
4 February 2026

REVISED
7 September 2026

ACCEPTED FOR PUBLICATION
1 October 2026

PUBLISHED
21 October 2026

Original content from this work may be used under the terms of the Creative Commons Attribution 4.0 licence.

Any further distribution of this work must maintain attribution to the author(s) and the title of the work, journal citation and DOI.

PAPER

Considering a long reference scale in photogrammetric bundle adjustment for evaluating gravity-induced focal length variation of a VGOS radio telescope

Michael Lösler[1,*], **Kira-Lynn Kopitzke**[2], **Cornelia Eschelbach**[1] and **Rüdiger Haas**[3]

[1] Laboratory for Industrial Metrology, Faculty 1: Architecture, Civil Engineering, Geomatics, Frankfurt University of Applied Sciences, Frankfurt am Main DE-60318, Germany
[2] Marpe Bau GmbH and Co. KG, Hauptstraße 40, DE-34477 Twistetal-Twiste, Germany
[3] Onsala Space Observatory, Department off Physics and Astronomy, Chalmers University of Technology, Onsala SE-439 92, Sweden
[*] Author to whom any correspondence should be addressed.

E-mail: loesler@fra-uas.de

Keywords: industrial photogrammetry, bundle adjustment, radio telescope, correlation, scale, deformation, laser tracker

Abstract

In industrial photogrammetry, the realization of the scale within a bundle adjustment affects the structure of the dispersion matrix of the estimated parameters and, consequently, the precision and reliability of derived quantities. This study investigates the effect of using a scale exceeding the object dimensions instead of several short scale bars. Photogrammetric measurements of a 13.2 m radio telescope were performed at the Onsala Space Observatory to investigate orientation-dependent, gravity-induced changes in the focal length of the main reflector. The data were analysed using a bundle adjustment constrained either by six 1.3 m scale bars or by introducing an additional 14.2 m scale measured in-process with two mobile laser trackers. While thermal expansion corrections were applied to all scales, the long scale could not be observed directly owing to the measurement configuration and therefore had to be realized indirectly. Its realization further required specific orientation-dependent corrections and a rigorous propagation of measurement uncertainties. The results show that introducing the long reference scale reduces the volume of the confidence regions of object points by approximately 50% and significantly decreases parameter correlations, with 68% of the estimated parameters exhibiting a reduction of at least 50%. Furthermore, the mean standard deviation of the estimated focal length is reduced by approximately 150 µm—an improvement of 40%. The results indicate that extrapolation effects associated with short scale bars are mitigated and long reference scales can substantially improve the precision and reliability of industrial photogrammetry applications in large-volume metrology, even when shorter scale bars provide higher intrinsic distance accuracy. Moreover, the impact of correlations is often underestimated in particular in subsequent applications where results of a prior adjustment are treated as incoming data. The results highlight the importance of accounting for stochastic dependencies in subsequent analyses.

1. Introduction

Industrial close-range photogrammetry is a widely used non-tactile approach for determining object coordinates. Using images taken from various perspectives, object coordinates and geometric properties are reconstructed by applying the fundamental collinearity equations. As the collinearity equations map the spatial coordinates onto corresponding planar image coordinates, the absolute scale is eliminated and remains indeterminate. Thus, photogrammetry is not a measurement system that inherently provides metric information, and external information defining the scale of length is required to trace the measurements back to the International System of Units (SI). Depending on the application and the accuracy requirements, the scale can be established using ground control points, reference objects

© 2026 The Author(s). Published by IOP Publishing Ltd

of known dimensions, or calibrated scale bars. Especially in industrial photogrammetry, high-precision scale bars are used to trace the measurements back to the SI metre. The lengths of these scale bars typically range from 10 cm to 2 m and feature uncertainties between 5 µm and 20 µm. As the camera acts as a medium transferring a known reference scale to the reconstructed object geometry, the measurement uncertainties primarily depend on the stability of the camera during this transfer, as well as on the length and reliability of the established scale in relation to the object dimension. Reznicek *et al* (2016) study the impact of the scale length in configurations similar to those used in aerial photogrammetry. The authors show that establishing short scale bars relative to the object's dimensions unsurprisingly leads to extrapolation errors, and therefore the authors recommend a long scale. Based on this result, Luhmann *et al* (2023), p655, suggest that a long scale of lower precision can outperform several highly precise short scale bars. Lösler *et al* (2025c) analyse photogrammetric data in the field of surface fitting and demonstrate the effect of short scale bars on the resulting correlations between object points obtained from a bundle adjustment. Strong correlations are particularly pronounced when short scales are used. If these correlations are neglected, derived quantities such as uncertainties or test statistics are biased and become unreliable. The use of long scale bars to reduce correlations, along with accounting for the fully populated dispersion matrix in subsequent applications, is strongly recommended. However, in large-volume metrology, the establishment of a sufficiently long scale is challenging. Kahmen and Luhmann (2016) propose a tensioned Invar wire to establish a long scale and demonstrate its effectiveness in improving the measurement results. Nevertheless, its applicability is limited, because tensioning a long wire in industrial environments is challenging, particularly when the object under investigation can be moved or rotated and must be measured in-process.

Radio telescopes used for very long baseline interferometry (VLBI) are fundamental instruments for space geodesy and Earth science. Their observations serve as basis for determining Earth orientation parameters, realize the celestial reference frame, and contribute to the realization of a global Earth-fixed geodetic reference frame (Schuh and Behrend 2012). Each radio telescope is equipped with a steerable parabolic main reflector with a diameter of several meters. This main reflector receives radio waves emitted by globally distributed quasi-stellar objects (quasars) and directs the signal to the telescope's focal point. Since the measurement principle of VLBI relies on signal travel-time measurements, the telescope's main reflector must be rigid and preserve a constant focal length. However, investigations of legacy VLBI radio telescopes indicate an orientation-dependent deformation behaviour of the main reflector induced by gravitational forces (e.g. Fu *et al* 2022, Lösler *et al* 2025a, Pfaffinger *et al* 2026). These deformations distort the beam path and systematically bias the obtained products. In particular, the determined vertical coordinate component is affected by gravity-induced deformations as shown by Sarti *et al* (2011). These systematic deformations can be corrected, if the orientation-dependent variation of the main reflector's focal length is known (Lösler *et al* 2019, Nothnagel *et al* 2019). For this purpose, the International VLBI Service for Geodesy and Astrometry (IVS) encourages investigations of radio telescopes to model gravity-induced deformations (IVS 2019).

This contribution investigates whether a reference scale exceeding the object dimensions can improve the reliability of photogrammetric bundle adjustments. A laser tracker-based realization of a long reference scale is applied to photogrammetric measurements of a VLBI radio telescope and compared with a solution based solely on short scale bars. The resulting parameter correlations, confidence regions, and uncertainties of derived quantities are analysed to evaluate the benefit of the long-scale approach.

2. Motivation

The Onsala Space Observatory is a Swedish research institution and co-location station hosting instruments for various space geodetic techniques. Three radio telescopes are operated for geodetic VLBI. Since 1979, the radome-enclosed 20 m radio telescope has participated in the legacy VLBI network. In 2017, two compact 13.2 m broadband radio telescopes were inaugurated and are operated in the network of the VLBI Global Observing System (VGOS). Both VGOS radio telescopes are identical in design (Haas *et al* 2019). Laser scanner based deformation measurements at the legacy radio telescope were performed in 2015 and revealed a focal length variation between 10 mm and 20 mm (Holst *et al* 2017, Bergstrand *et al* 2019). The surface deformation of the northeastern VGOS radio telescope (ONSA13NE) was photogrammetrically investigated in 2018. Lösler *et al* (2019) derived a focal length variation of about 2 mm, which is an order of magnitude smaller than that of the legacy radio telescope, indicating the advantages of the compact design. Due to their identical design, the deformation behaviour is assumed to be the same for both VGOS radio telescopes (Varenius *et al* 2021). This assumption, however, has not yet been

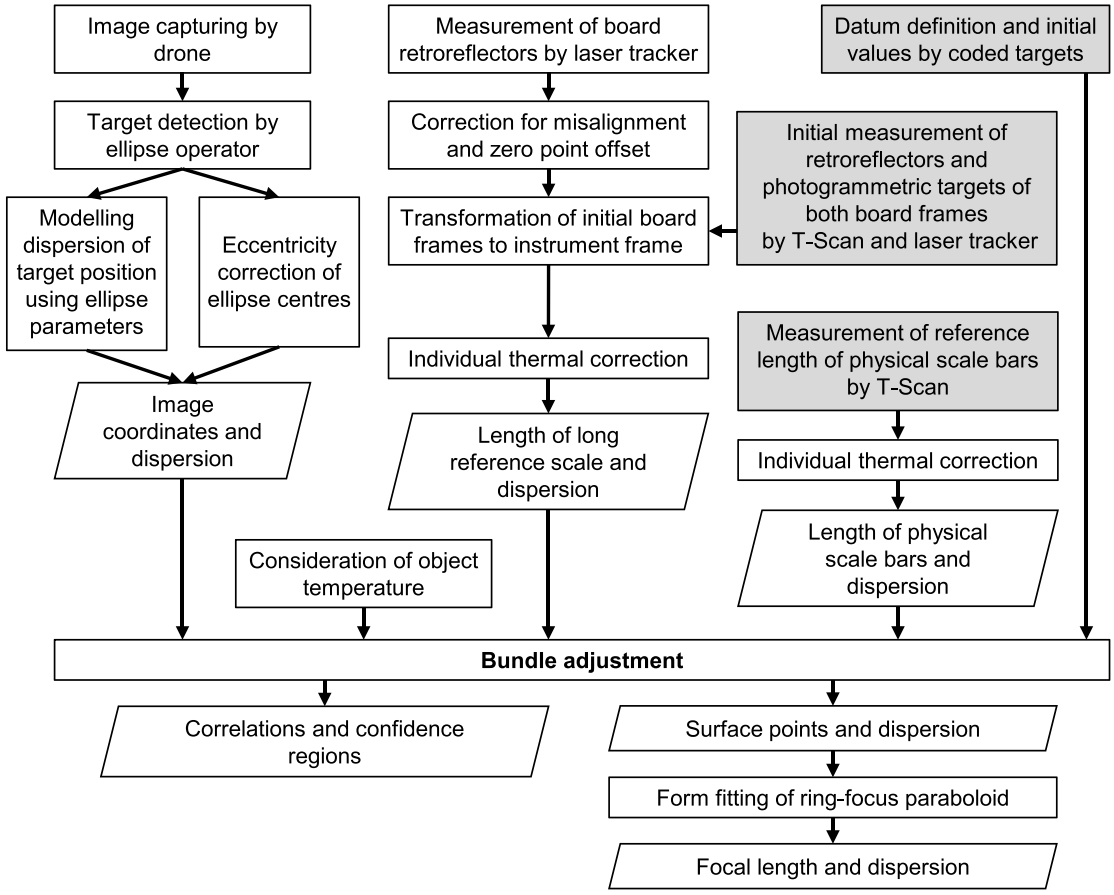

Figure 1. Schematic illustration of the workflow; white elements are performed for each telescope orientation, while grey elements need to be carried out only once. For all steps rigorous variance-covariance propagation is applied in accordance with JCGM100 (2008), JCGM102 (2011).

verified—and is the motivation to investigate the southwestern VGOS radio telescope (ONSA13SW) in this contribution.

In order to investigate the deformation of the main reflector of ONSA13SW and to assess whether the results obtained from the VGOS twin telescope are transferable, a measurement campaign was conducted in 2025. For that purpose, the main reflector surface was surveyed by means of close-range photogrammetry. Six physical 1.3 m scale bars were mounted on the rim of the main reflector, the supporting struts for the sub-reflector, and close to the focal point, to trace the measurements back to SI. As the capabilities of photogrammetric systems and laser trackers have been well established in large-volume industrial metrology (e.g. Martin *et al* 2016, Wu *et al* 2024, Lösler *et al* 2025b), two mobile laser trackers were employed to realize a 14.2 m scale exceeding the diameter of the main reflector. Thus, investigating the advantage of a long reference scale on the results is the further motivation of this contribution.

Figure 1 shows an overview of the performed workflow. A detailed description of each step is presented throw the following sections. Section 3 briefly presents the photogrammetric measurement concept used to survey the main reflector surface of the VLBI radio telescope. Section 4 deals with the reference scales mounted on the main reflector. In addition to the 1.3 m scale bars, the concept of realizing a process-integrated long 14.2 m reference scale is presented. Section 5 introduces the bundle adjustment, focusing on the stochastic model as well as the correction of eccentricity errors of circular object targets. The mathematical model of the ring-focus paraboloid is briefly described in section 6. The analysis results are presented and discussed in section 7. Finally, section 8 concludes this investigation.

3. Measurement concept

The VGOS radio telescopes at the Onsala Space Observatory were inaugurated in 2017, and have been operating in regular IVS VGOS sessions since early 2019 (Varenius *et al* 2021). Both broadband radio telescopes use an azimuth-elevation mount and are identical in design (Haas *et al* 2019). The main



Figure 2. Prepared VGOS radio telescope (ONSA13SW) at the Onsala Space Observatory with detail views. The main reflector as well as the sub-reflector are equipped with circular black-and-white targets. Six physical scale bars, highlighted by red rectangles, are mounted on the rim, the supporting struts, and the sub-reflector. The long reference scale exceeding the main reflector's diameter is realized by two boards mounted diametrically opposite each other. Both boards are highlighted by yellow hexagons. Eight temperature sensors are mounted at the back-end structure of the main reflector. The sensor positions are indicated by purple circles. A drone capturing images is visible in front of the telescope. Detail views show a 1.3 m scale bar, a temperature sensor, and the front and back of a prepared board.

reflector has a diameter of 13.2 m and is designed as a ring-focus paraboloid to reduce regions of decreased intensity. The reflector is composed of 60 aluminium panels arranged in three concentric rings. The outer and middle rings consist of 24 panels each, while the inner ring is made up of 12 panels. These panels are supported by a steel back-end structure that provides the overall ring-focus paraboloid shape. Following the procedure proposed by Lösler *et al* (2019, 2022a), circular black-and-white targets with a diameter of 46 mm were used to materialize surface points for the photogrammetric measurement. Each panel of the outer ring was equipped with four uncoded targets located near the corners, while each panel of the middle and inner rings was equipped with three uncoded targets, following the isosceles trapezoidal panel design. These 204 uncoded targets served to investigate gravity-induced deformations of the main reflector. To pre-orient the surface points and to derive initial approximations for each camera's position and orientation, 22 uniquely coded circular black-and-white targets were evenly mounted on the surface. The sub-reflector was equipped with 14 additional coded targets to improve the spatial distribution of the measured points and to increase the reliability of the adjustment results. During the bundle adjustment, the coded targets define the datum of the object-based reference frame and were used to formulated the minimum inner constraints of the free network adjustment (see Granshaw 1980, Lösler *et al* 2021). Figure 2 shows the VGOS radio telescope equipped with 240 targets together with the drone capturing photogrammetric images during an experiment.

The main reflector of the VGOS radio telescope was photogrammetrically observed in elevation angles from 10° to 90° in steps of 10°, as well as at 6° elevation. For image capturing, a Sony ILX-LR1 camera equipped with a 35 mm lens was gimbal-mounted on the drone. The experiments were conducted at different azimuths to optimize the illumination of the surface by sunlight. During an experiment, the camera settings remained unchanged. Small variations in illumination between different experiments were compensated by adapting the sensor sensitivity, i.e. the ISO number. Different flight paths were evaluated with respect to the reliability of the estimated focal length by analysing simulated configurations utilizing the first-order network design optimization (e.g. Koch 1985). The optimized flight path of the drone capturing images consisted of three concentric circles around the principal axis of the main reflector. The circle radii and the corresponding distances along the principal axis, measured from the main reflector's rotation point, are summarized in table 1.

Each experiment took about 6 min and was carried out several times. However, immediate repetitions were largely avoided to prevent possible unforeseen time-dependent effects. In total, about 100 experiments were carried out within four days. Images were taken with a frequency of 1 Hz resulting in total number of about 350 images per experiment. The exposure time was set to 0.5 ms. According to Luhmann *et al* (2023), p614, this short exposure time combined with the low flight speed resulted in

Table 1. Flight path configuration and velocities of the experiments.

Circle	i	ii	iii
Radius	3 m	6 m	12 m
Distance	24 m	22 m	18 m
Velocity	0.2 m s^{-1}	0.4 m s^{-1}	0.45 m s^{-1}

a negligible image blur of approximately 0.1 px, well below the tolerable limit of 1 px for close-range photogrammetry.

In order to be able to account for temperature changes in the structure during the data analysis of the experiments, eight evenly distributed MSR145 contact temperature sensors were mounted on the back-end structure of the main reflector, as indicated in figure 2. The measurement uncertainty of the temperature is specified as 0.1 K (MSR 2024).

4. Reference scales

Six physical 1.3 m carbon scale bars covering the measurement volume were used to trace the measurements back to SI. As shown in figure 2, three scale bars were evenly mounted on the rim of the main reflector, one on the sub-reflector, and two on the supporting struts. This object-enclosed uniform distribution is chosen to minimizes extrapolation deviations. To establish a scale exceeding the main reflector's diameter, two aluminium boards were attached diametrically opposite on the rim. Each board was equipped with two coded targets on the front side and seven 1.5" retroreflectors on the back side, as shown in the detail views on the right hand side of figure 2. One of the coded targets was glued approximately at the centre of mass of the retroreflectors to minimize the impact of extrapolation errors during the transformation procedure described in section 4.2. The second coded target was a backup target that could be used if the first target was damaged or unreadable. Moreover, contact temperature sensors were attached to two of the six plates as well as to both boards to account for temperature changes in the material during data analysis. Temperature values were automatically recorded every 20 s.

4.1. Physical scale bars

A physical scale bar consists of a 1 m carbon bar with two 200 mm × 200 mm aluminium plates. The plates are screwed to either end of the bar, and each plate is equipped with a uniquely coded target, as shown in figure 2. The scale bars were transported in disassembled components. The screw connections between the components lead to minor variations in length, necessitating a post-assembly determination of the reference lengths at the observatory. The reference length of a scale bar, defined as the distance between the centres of the circles, was derived by scanning both targets with Leica's T-Scan. The measurement uncertainty of a spatial length is specified as 30 µm (Hexagon 2015b). Due to the uniformly high contrast, the circular edge could be reliably reconstructed from changes in the intensity of the reflected laser beam. For each circle, about 4500 edge points were detected, and the circle centre was reliably determined by means of an orthogonal distance fit. The length of each scale bar was measured on the ground under controlled environmental conditions over several days prior to the surveying flights. According to equation (1), temperature changes between the measurements, as well as differences in the materials' coefficients of thermal expansion, were taken into account. In total, more than 30 repetitions were performed, yielding standard deviations between 15 µm and 20 µm, and is therefore consistent to the specification. The mounting of the scale bars is not entirely free of strain. However, the maximum bending was assessed to be $\Delta = 1$ mm. As the bending Δ is small compared to the length $s = 1.3$ m of the scale bar ($\Delta \ll s$), the change in length ∇ can be appropriately expressed as the difference between the arc length and the chord length using the circular-segment relation and reads

$$\nabla = \frac{8\Delta^2}{3s} \approx 2\,\mu\text{m}.$$

Thus, the resulting change of 2 µm is negligible.

During the flight experiments, changes in material temperature were monitored by two attached contact temperature sensors, allowing for correction of the corresponding expansion of the scale bars. The expansion correction is given by

$$\Delta s = -\left(2\,l_{\mathrm{Pl}}\,\gamma_{\mathrm{Al}} + l_{\mathrm{Cb}}\,\gamma_{\mathrm{C}}\right)\left(T - T_0\right), \tag{1}$$

where $\gamma_{\mathbf{Al}} = 2.31 \times 10^{-5}\mathrm{K}^{-1}$ and $\gamma_{\mathbf{C}} = -1 \times 10^{-6}\mathrm{K}^{-1}$ denote the coefficients of thermal expansion for aluminium and carbon, respectively. The distance from the edge to the target glued on a plate is $l_{\mathbf{Pl}} = 175$ mm. The length of the carbon bar is $l_{\mathbf{Cb}} = 1000$ mm. The reference temperature was set to $T_0 = 9\,^{\circ}\mathrm{C}$ in accordance with the value used in VLBI analysis (Nothnagel 2025), and $(T - T_0)$ denotes the change in temperature w.r.t. T_0.

4.2. Long reference scale

The coded targets glued to the front side of both boards define the long reference scale of about 14.2 m and were captured by the drone during each experiment, as shown in figure 2. In contrast to the physical scale bars, which were measured prior to the surveying flights, the long reference scale must be measured in-process, because the boards were mounted on the telescope structure, which may deform at different telescope orientations. The 1.5" retroreflectors magnetically mounted on the back side of the boards were independently observed by Hexagon's mobile laser trackers AT401 and AT960. The manufacturer specifies the maximum permissible error of a statically observed position as $15\ \mu\mathrm{m} + 6\ \mu\mathrm{m\,m}^{-1}$ for both instruments (Hexagon 2012, 2015a). As the boards co-rotate with the main reflector and to prevent any obstruction of the line of sight by the co-rotating counterweights of the radio telescope, the instruments were positioned behind the telescope as indicated in figure 3(a). This configuration enables simultaneous measurements of the retroreflectors of both boards from a single station and avoids stationing uncertainties. Moreover, the telescope casts a shadow over the instruments and protects them from direct sunlight. Meteorological environmental parameters were registered by external sensors, and the first velocity correction was applied according to the manufacturer's recommendations (Hexagon 2021).

As shown in figure 3(b), the acceptance angle of retroreflectors restricts the possible instrument locations. Typical 1.5" glassless spherically mounted retroreflectors (SMR) used in laser tracker applications are limited to $\pm 30°$, i.e. a range of the incidence angle of 60°. In contrast to an SMR, glass-body retroreflectors offer an acceptance angle of $\pm 45°$. For this purpose, 1.5" spherically mounted glass-body retroreflectors (SGR) manufactured by Bohnenstingl (S/N: 1445.SN) were used, and the distance between the telescope monument and the instruments was restricted to a range between 4 m and 10 m. The retroreflectors were initially aligned with the instrument's line of sight at an elevation angle of 45°, with a retroreflector temporarily placed in front of the mounted SGR being observed. This paired observation of both retroreflectors yields the position $\mathbf{X}_{\mathrm{INI}}$ and the related normalized alignment vector $\mathbf{n}_{\mathrm{INI}}$ of each mounted SGR.

4.2.1. Retroreflector corrections

A misaligned SGR causes systematic radial ε_r and lateral ε_l deviations as a consequence of the different refractive indices of air n_{A} and glass n_{G}. Both refractive indices depend on the instruments wavelength. According to Pauli (1969), Rüeger (1978), the radial and lateral deviations can be expressed as functions of the angle of incidence α and are given by

$$\varepsilon_r(\alpha) = a\left(\frac{n_{\mathrm{G}}}{n_{\mathrm{A}}} - \sqrt{\frac{n_{\mathrm{G}}^2}{n_{\mathrm{A}}^2} - \sin^2(\alpha)}\right) - b\,(1 - \cos(\alpha))\,, \tag{2a}$$

$$\varepsilon_l(\alpha) = (a - b)\sin(\alpha) - a\sec(\alpha_{\mathrm{G}})\sin(\alpha - \alpha_{\mathrm{G}}), \tag{2b}$$

respectively, where $\sin(\alpha_{\mathrm{G}}) := \frac{n_{\mathrm{A}}}{n_{\mathrm{G}}}\sin(\alpha)$. The dimensions of the retroreflector are defined by the height of the prism apex a and the distance between the surface front and the prism centre b as indicated in figure 4 (Rüeger 1996, p156).

Based on laboratory investigations, Lösler *et al* (2026) derived individual zero-point offsets referring to the laser tracker's wavelength, as well as the dimensional parameters a and b of the prism by means of a least squares adjustment, cf figure 5. Each SGR used is certified with a zero-point offset of $\tilde{c} = -17.0\,\mathrm{mm}$. Figure 5(a) depicts the individually determined zero-point offsets c of the 14 retroreflectors w.r.t. the reference SMR as red dots. The retroreflectors were measured six times, with each SGR rotated by approximately 60° about the surface normal after each distance measurement. The mean standard deviation is 5 µm, which indicates the high repeatability of the measured offsets. However, the offsets vary by 0.1 mm and differ significantly from the certified value, necessitating individual corrections. Figure 5(b) shows the observed lateral and radial deviations of the retroreflectors as orange squares and blue dots, respectively, along with the derived correction functions. The estimated dimensional parameters are $\hat{a} = 19.80 \pm 0.05\,\mathrm{mm}$ and $\hat{b} = 12.65 \pm 0.03\,\mathrm{mm}$. The radial deviations do not exceed 0.3 mm, and can be interpreted as an additional incident angle-dependent zero-point offset. The lateral deviations are

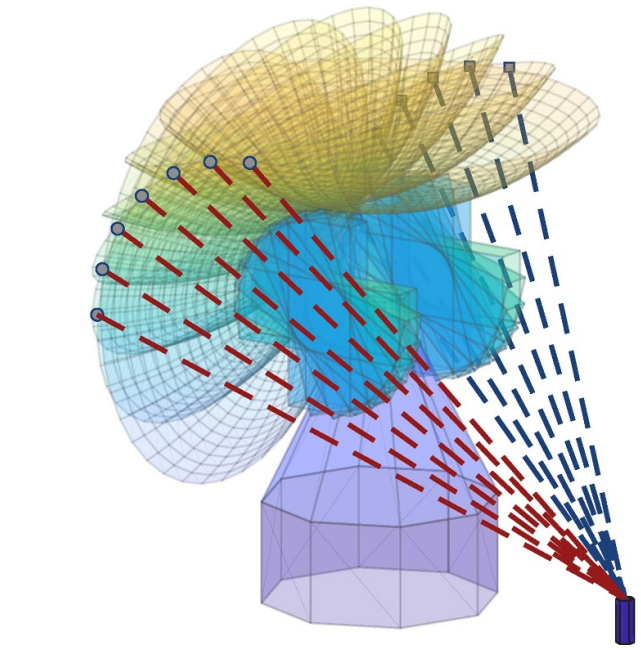

(a) Line of sight verification

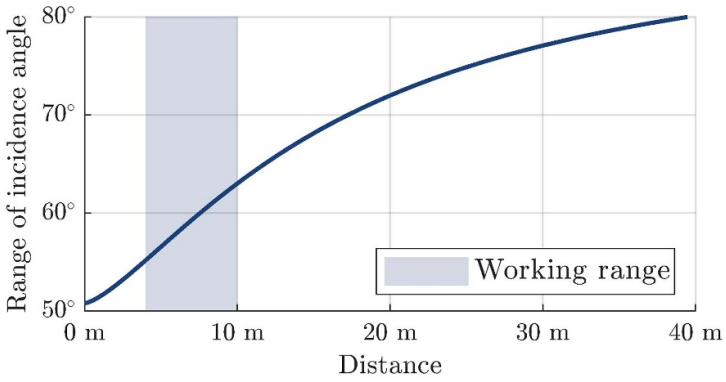

(b) Range of incidence angle vs. distance

Figure 3. Evaluation of measurement configuration. (a) Verification of the visibility of co-rotating retroreflectors at the main reflector of the radio telescope from the instrument location. (b) Range of incidence angles depicted as a function of the distances from the telescope to the laser tracker. The blue area indicates the designated operational range for the laser tracker.

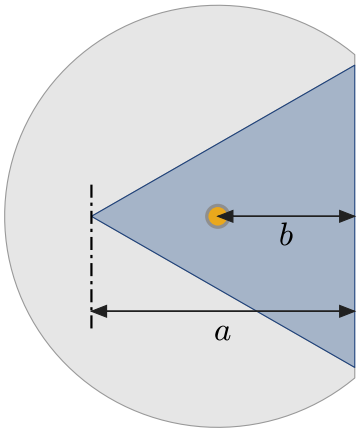

Figure 4. Definition of the dimensional parameters *a* and *b* of a spherically mounted glass-body retroreflector. The glass-body prism is shown in blue, while the spherical housing is shown in grey. A yellow dot corresponds to the centre.

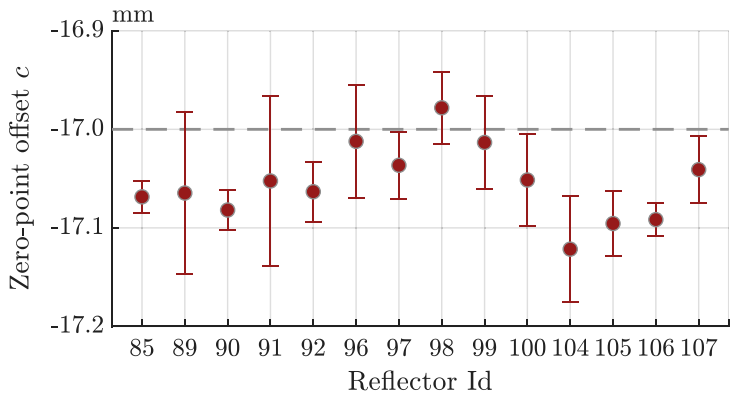

(a) Zero-point offsets

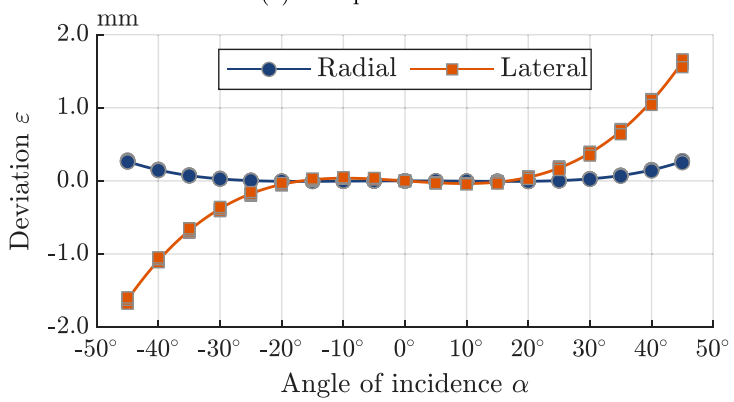

(b) Radial and lateral deviations

Figure 5. Derived SGR corrections for zero-point offsets as well as radial and lateral deviations. (a) Red dots indicate the individually determined zero-point offset of each 1.5" SGR. The error bars are scaled at a ratio of 10:1. The dashed grey line indicates the certified value. (b) Derived functions of radial (blue) and lateral (orange) deviations. Blue dots and orange squares correspond to observed values.

one order of magnitude larger, and a misalignment of, for example, 40° leads to a deviation of 1 mm. Both deviations need to be taken into account.

The incidence angle α depends on the alignment of the retroreflector, the position of the instrument, and the telescope orientation defined by the elevation angle ϵ. The angle α was derived from a rigid body transformation of the board using a generalized least square approach (e.g. Wu *et al* 2025, Lehmann and Lösler 2026). Let $\mathbf{X}_\diamond$ denote the translation vector, and ϕ, ξ, and d the polar observations of an observed point in the present configuration, the transformation is given by

$$(d+c)\,\mathbf{n}_{\mathrm{SGR}} = \mathbf{R}_\diamond^\top\,(\mathbf{X}_{\mathrm{INI}} - \mathbf{X}_\diamond)\,, \tag{3}$$

where the orthogonal matrix $\mathbf{R}_\diamond$ defines the rotational sequence. The line of sight $\mathbf{n}_{\mathrm{SGR}}$, defined between the instrument and the SGR being observed, reads

$$\mathbf{n}_{\mathrm{SGR}} = \begin{pmatrix} \sin(\phi)\,\sin(\xi) \\ \cos(\phi)\,\sin(\nu) \\ \cos(\xi) \end{pmatrix}, \tag{4}$$

where ϕ and ξ denote the horizontal and vertical angles, respectively. According to figure 6, the angle of incidence is readily obtained from

$$\cos(\alpha) = -\mathbf{n}_{\mathrm{SGR}}^\top \mathbf{R}_\diamond^\top \mathbf{n}_{\mathrm{INI}}. \tag{5}$$

The individual zero-point offset and the radial deviation were applied directly to the meteorologically corrected distance d. However, separating and directly applying the lateral correction to the polar observations ϕ and ξ is challenging. Hence, the alignment vector of the observed SGR was orthogonally

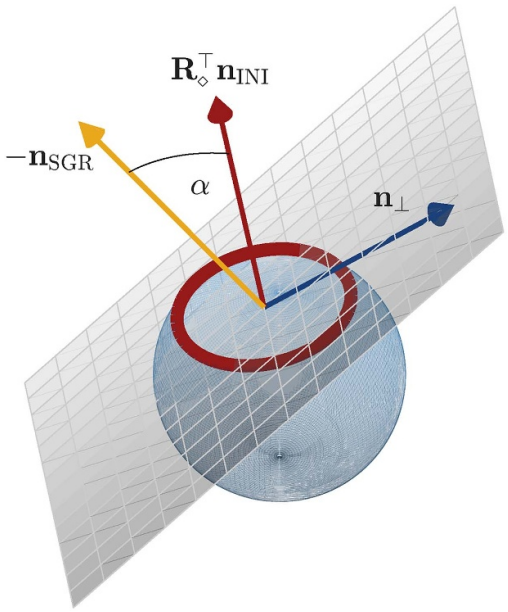

Figure 6. Angle of incidence α derived from the yellow vector $\mathbf{n}_{\mathrm{SGR}}$ of the line of sight and the red alignment vector of the retroreflector denoted by $\mathbf{R}_{\diamond}^{\top}\,\mathbf{n}_{\mathrm{INI}}$. The orthogonal projected alignment vector $\mathbf{n}_{\perp}$ is depicted in blue and lies in the grey plane defined by $\mathbf{n}_{\mathrm{SGR}}$.

projected onto the subspace orthogonal to the vector $\mathbf{n}_{\mathrm{SGR}}$ of the line of sight as shown in figure 6. The projected vector reads

$$\mathbf{n}_{\perp} = \mathbf{R}_{\diamond}^{\top}\,\mathbf{n}_{\mathrm{INI}} - \left(\mathbf{n}_{\mathrm{SGR}}^{\top}\mathbf{R}_{\diamond}^{\top}\,\mathbf{n}_{\mathrm{INI}}\right)\mathbf{n}_{\mathrm{SGR}}, \tag{6}$$

and the total correction applied to the observed SGR position in the instrument frame is given by

$$\mathbf{X} = (d + c + \varepsilon_r(\alpha))\,\mathbf{n}_{\mathrm{SGR}} + \varepsilon_l(\alpha)\,\frac{\mathbf{n}_{\perp}}{\|\mathbf{n}_{\perp}\|_2}. \tag{7}$$

Applying variance-covariance propagation as proposed by JCGM102 (2011), p15, yields the corresponding dispersion matrix for the observed retroreflectors on the boards. The correction procedure has been successfully verified under laboratory conditions prior to the measurement campaign using a long reference scale. For a detailed description, the interested reader is referred to Kopitzke (2026).

4.2.2. Length of scale

To determine the length of the scale, the retroreflectors mounted on the board's back side and both coded targets glued on the front side were jointly observed on the ground under controlled environmental conditions. For this purpose, each board was equipped with additional glassless retroreflectors temporarily mounted on both sides, and observed from different perspectives using the AT960. The retroreflectors were measured directly, while the coded targets were scanned with Leica's T-Scan. The coordinates $\overline{\mathbf{X}}$ of the retroreflectors and coded targets were determined in a consistent board coordinate frame, together with the corresponding fully populated dispersion matrix, using the software package Java·Applied·Geodesy·3D (JAG3D 2025).

The translation vector $\mathbf{X}_{\triangle}$ and the rotation matrix $\mathbf{R}_{\triangle}$, which transform points from a board frame to the current instrument frame, were derived by a general least squares adjustment defining the parameters of the rigid body transformation. The dispersion matrices of $\mathbf{X}$ and $\overline{\mathbf{X}}$ form the stochastic model within the adjustment procedure to ensure rigorous uncertainty propagation. Based on these parameters, the positions of the coded targets were transformed accordingly using

$$\mathbf{X} = \mathbf{R}_{\triangle}^{\top}\left(\overline{\mathbf{X}} - \mathbf{X}_{\triangle}\right). \tag{8}$$

The length of the scale is defined between the centred coded targets $\mathbf{X}_{\mathrm{I}}$, $\mathbf{X}_{\mathrm{II}}$ of both boards, and was obtained from

$$s_0 = \|\mathbf{X}_{\mathrm{I}} - \mathbf{X}_{\mathrm{II}}\|_2. \tag{9}$$

The correction of the temperature-dependent expansion of the long reference scale s_0 depends on the changes in material temperature of the boards $(T_{\mathrm{Bo}} - T_0)$ as well as that of the telescope's back-end structure $(T_{\mathrm{Bs}} - T_0)$. Both were monitored by ten attached temperature sensors. The expansion-corrected length w.r.t. to the reference temperature $T_0 = 9°\mathrm{C}$ is given by

$$s = s_0 - 2\,l_{\mathbf{Bo}}\,\gamma_{\mathbf{C}}\,(T_{\mathrm{Bo}} - T_0)\,\gamma_{\mathbf{Al}} - l_{\mathbf{Bs}}\,\gamma_{\mathbf{St}}\,(T_{\mathrm{Bs}} - T_0)\,, \tag{10}$$

where $l_{\mathbf{Bs}} \approx 13.2$ m denotes the distance between the mounting points of the boards through the back-end structure and $\gamma_{\mathbf{St}} = 1.2 \times 10^{-5}\,\mathrm{K}^{-1}$ is the coefficient of thermal expansion for steel. The distance from the edge to the centred target glued on a board is $l_{\mathbf{Bo}} = 500$ mm. The lengths derived from both laser tracker measurements deviate by a few micrometres within an experiment, thus, the averaged value was used for data analysis. According to JCGM102 (2011), p15, the corresponding standard deviation resulted from variance-covariance propagation applied to equations (7)–(10). The mean standard deviation is 70 µm and about five times larger than for the short physical scale bars.

5. Bundle adjustment

The photogrammetric bundle adjustment is a commonly used method to derive object coordinates from images taken from various perspectives. The following subsections recapitulate the principle of the bundle adjustment as part of the uncertainty chain. The consideration of reference lengths and an improved stochastic model are discussed. Besides the parameters to be estimated, the fully populated dispersion is obtained, providing essential information about the reliability and precision of the adjustment results. The estimates are obtained by integrating the functional and stochastic models within a least squares adjustment.

5.1. Functional model

A spatial coordinate transformation consisting of a translation $\mathbf{x}_\star$, a rotation $\mathbf{R}_\star$ and a scale $\mu_\star$ describes the relation between two congruent coordinate systems via

$$\mathbf{x}^* = \frac{1}{\mu_\star}\mathbf{R}_\star^\top\,(\mathbf{x} - \mathbf{x}_\star)\,, \tag{11}$$

where $\mathbf{x}$ and $\mathbf{x}^*$ are corresponding coordinates in the respective systems. Let the vector be $\mathbf{x}^* = \begin{pmatrix} x^* & y^* & c^* \end{pmatrix}^\top$, the well-known collinearity equations are obtained by dividing the first two equations by the third equation and read (e.g. Luhmann *et al* 2023, p269)

$$x^* = c^*\,\frac{\mathbf{r}_1^\top\,(\mathbf{x} - \mathbf{x}_\star)}{\mathbf{r}_3^\top\,(\mathbf{x} - \mathbf{x}_\star)}, \tag{12a}$$

$$y^* = c^*\,\frac{\mathbf{r}_2^\top\,(\mathbf{x} - \mathbf{x}_\star)}{\mathbf{r}_3^\top\,(\mathbf{x} - \mathbf{x}_\star)}, \tag{12b}$$

where the principal distance is c^*, the projection centre is $\mathbf{x}_\star$, and $\mathbf{r}_i$ denotes the ith column vector in $\mathbf{R}_\star$.

The collinearity equations map the spatial position $\mathbf{x}$ of an object point onto the two-dimensional image plane utilizing the central projection. Due to deviations of the optical path of the camera from the principle of the central projection, the observed planar image coordinates x', y' are shifted by the principal point x_0, y_0, and are affected by radial and tangential decentring distortions as well as affine and shear effects of the sensor (see Dold 1997, Godding 2017). Summarizing the distortion parameters by Δx, Δy, the observed image coordinates are given by

$$\begin{pmatrix} x' \\ y' \end{pmatrix} = \begin{pmatrix} x'_0 \\ y'_0 \end{pmatrix} + \begin{pmatrix} x^* \\ y^* \end{pmatrix} + \begin{pmatrix} \Delta x \\ \Delta y \end{pmatrix}. \tag{13}$$

Substituting equation (12) into equation (13) yields the observation equations of the photogrammetric bundle adjustment, allowing for an *in-situ* calibration of the camera.

From equation (12) it is easy to verify that the scale $\mu_\star$ is eliminated. As the object points are parameters to be estimated, external information defining the scale is required. Typically, reference lengths

$$s_{ij} = \left\|\mathbf{x}_i - \mathbf{x}_j\right\|_2 \tag{14}$$

between object points are introduced as additional observation equations, thereby providing a scale of length for the determination of object coordinates.

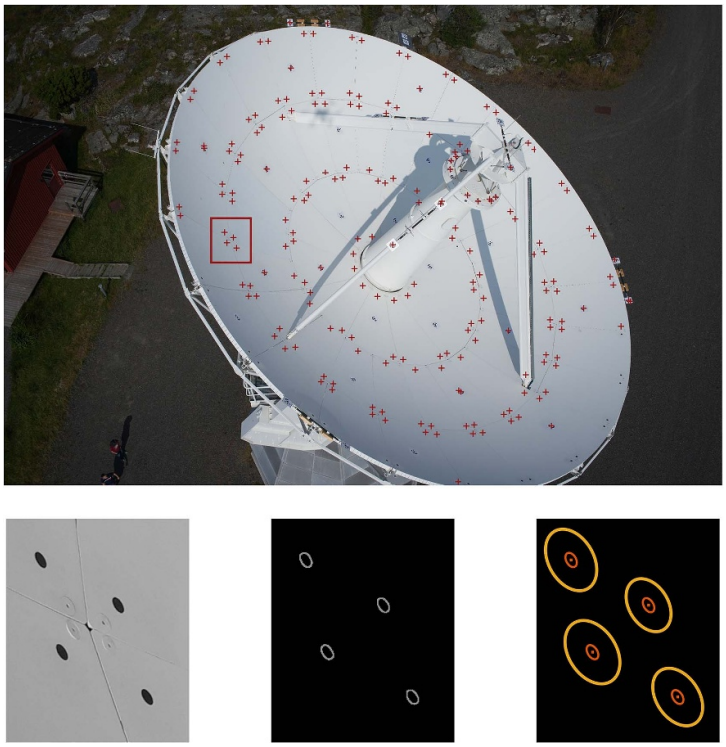

Figure 7. Circular target recognition for coded and uncoded targets. For an arrangement of four targets, the recognition procedure is illustrated in detail. The detail images show (from left to right): the greyscale image, the detected edges of the binary image, and the best-fit ellipses (red) of the targets together with the confidence ellipses (yellow) of the estimated centres.

5.2. Stochastic model

Whereas the functional model of the bundle adjustment describes the mapping of the parameters to be estimated onto the observations, the stochastic model characterizes the statistical dispersion of these observations. The planar image coordinates of the circular target centres serve as the photogrammetric observations. These planar image coordinates are usually assumed to be identically and independently distributed, and the corresponding stochastic model becomes a scaled unit matrix (e.g. Granshaw 1980, Grün 1982, Fraser *et al* 2005). However, when using circular targets, this assumption becomes an oversimplification. Hence, a refined stochastic model that incorporates the individual dispersion of each detected target centre was employed.

Under appropriate conditions, a projected circular target appears as an ellipse in the image. By applying an edge detection approach (e.g. Canny 1986, Deriche 1987), the contour of the projected ellipse is extracted (e.g. Xie and Ji 2002, Yu *et al* 2015). The centre, the semi-axes, as well as the orientation angle of the ellipse are determined from the contour points x_i, y_i, as illustrated in figure 7. An arbitrarily oriented ellipse with angle ϕ is given by

$$E(x_i, y_i) = \begin{pmatrix} x_i - x_c' \\ y_i - y_c' \end{pmatrix}^\top \mathbf{R}_\phi \begin{pmatrix} a_1^2 & 0 \\ 0 & a_2^2 \end{pmatrix}^{-1} \mathbf{R}_\phi^\top \begin{pmatrix} x_i - x_c' \\ y_i - y_c' \end{pmatrix} = 1, \tag{15}$$

where x_c', y_c' denote the centre, a_1, a_2 are the semi-axes, and the orthogonal rotation matrix reads

$$\mathbf{R}_\phi = \begin{pmatrix} \cos(\phi) & -\sin(\phi) \\ \sin(\phi) & \cos(\phi) \end{pmatrix}. \tag{16}$$

Substituting

$$\begin{aligned} x_i - x_c' &= a_1 \cos(\phi)\cos(t_i) - a_2 \sin(\phi)\sin(t_i), \\ y_i - y_c' &= a_1 \sin(\phi)\cos(t_i) + a_2 \cos(\phi)\sin(t_i) \end{aligned}$$

into equation (15) yields the parametric representation of the ellipse with parameter $t_i \in [0, 2\pi)$, i.e.

$$E(t_i) = \frac{a_1^2 \cos^2(t_i)}{a_1^2} + \frac{a_2^2 \sin^2(t_i)}{a_2^2} = 1. \tag{17}$$

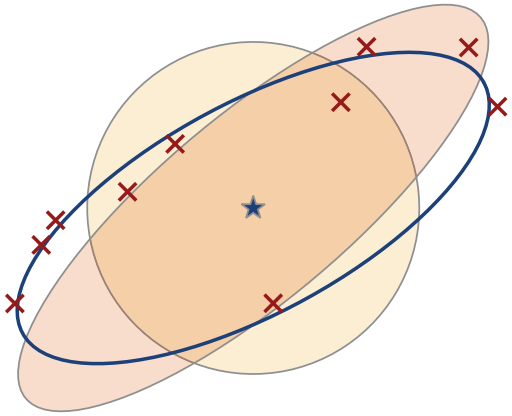

Figure 8. Comparison of the best-fit ellipse (blue curve) derived from ten points (red crosses) and the confidence ellipse of the centre (light red area). The yellow circle corresponds to a confidence circle for independent and identically distributed coordinates. The area of the circle and both ellipses is identical.

The observed contour points can be assumed to be independent and identically distributed, because a black-and-white target exhibits a uniformly high contrast. Moreover, given n contour points x_i, y_i with t_i being uniformly spaced in $[0, 2\pi)$, the confidence ellipse of the centre is self-similar to the original ellipse. After some lengthy algebraic manipulations, the dispersion matrix of the centre can be expressed as

$$\boldsymbol{\Sigma}' := \sigma_0^2 \mathbf{R}_\phi \begin{pmatrix} a_1^2 & 0 \\ 0 & a_2^2 \end{pmatrix} \mathbf{R}_\phi^\top . \tag{18}$$

Here, the variance of the unit weight is denoted by σ_0^2. During the adjustment procedure, the choice of σ_0^2 does not affect the parameters to be estimated as only relative weights are relevant. Thus, the confidence ellipse of the centre is identically oriented and has semi-axes proportional to those of the original ellipse. The coordinates of the centre are independent and identically distributed if the circular target is projected as a circle with $a_1 = a_2$ in the image plane, i.e. if the target plane and the image plane are coplanar. A complete derivation of equation (18) is given in appendix.

As most circular target recognition approaches return the ellipse parameters instead of the contour points, the dispersion can be readily reconstructed. Even if a uniform distribution of t is not fulfilled, equation (18) provides a suitable approximation of the dispersion in most practical applications. Figure 8 shows a comparison between the best-fit ellipse derived from ten points, the confidence ellipse of the estimated centre, and a confidence circle that represents independent and identically distributed coordinates. Whereas the best-fit ellipse provides an appropriate approximation of the confidence ellipse of the centre, the circle deviates significantly and represents an oversimplification. With an increasing number of almost uniformly distributed points, the best-fit ellipse and the confidence ellipse become asymptotically congruent, cf figure 7.

The ellipse centres are stochastically independent of each other, as the contour points are assumed to be independent random variables. Thus, the dispersion matrix defining the stochastic model of the bundle adjustment has a block-diagonal structure, consisting of the dispersion $\boldsymbol{\Sigma}'$ of each centre as well as of the variances of the scales.

5.3. Eccentricity of ellipse centre

Under appropriate conditions, the conic section of a projected circular target appears as an ellipse in the image plane, if the target plane and the image plane are not coplanar. Due to the geometrical properties of the central projection, the projected centre x', y' of the target does not necessarily coincide with the ellipse centre x'_c, y'_c of the projected contour of the target (Dold 1996). Figure 9 depicts the difference between both centres. This difference, also known as eccentricity, represents a systematic error. As discussed by Liebold and Maas (2024), small targets and camera perspectives that are almost perpendicular to the target plane minimize this error during the bundle adjustment. However, the impact of the eccentricity onto the adjustment results is hard to predict and a generally applied correction is recommended (Ahn *et al* 1999).

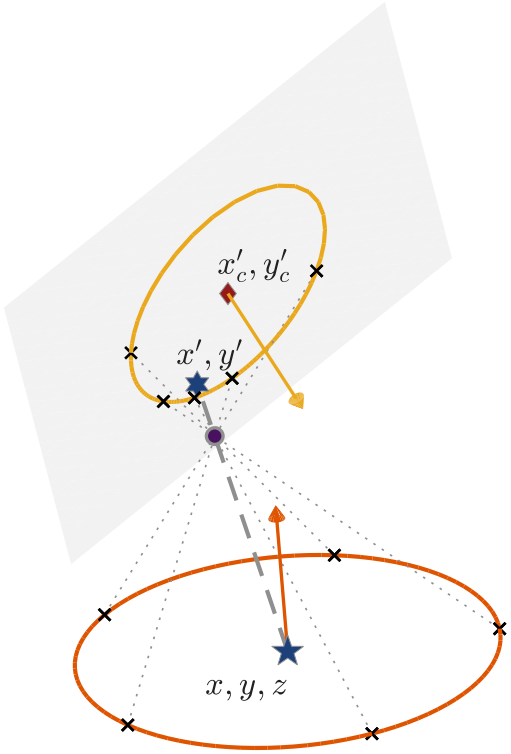

Figure 9. Projection of a circular target (orange) onto the image plane (grey). The projected image appears as an ellipse (yellow). The centre of the ellipse, derived from the projected edge points, is indicated by a red diamond. The centre of the original target and its projection are shown in blue as a star and a hexagram, respectively. The orange and yellow arrows correspond to the normal vectors of the target plane and the image plane, respectively.

Let the target radius be known. A common approach, also used in this investigation, is based on a two-step procedure indicated in figure 9. An initial bundle adjustment is performed without eccentricity correction. Based on this initial result, the target centres are estimated and the corresponding target planes are subsequently reconstructed using projective geometry (see Safaee-Rad *et al* 1992). The contour of a target is derived using the target radius. Both the contour and the centre of the target are projected onto the image plane using equation (13), and the ellipse centre is derived from the projected contour. The eccentricity is given by the difference vector

$$\begin{pmatrix}\delta x'\\ \delta y'\end{pmatrix} = \begin{pmatrix}x'\\ y'\end{pmatrix} - \begin{pmatrix}x'_c\\ y'_c\end{pmatrix} \tag{19}$$

between the projected target centre and the ellipse centre. A direct estimation procedure yielding the eccentricity correction is proposed by Otepka and Fraser (2004). Once the correction has been applied, the bundle adjustment is performed and—if necessary—the process is iterated.

6. Ring-focus paraboloid

The aim of this study is to investigate gravity-induced changes in the focal length Δf of the radio telescope. In contrast to legacy radio telescopes, which are mostly equipped with a main reflector defined by a rotationally symmetric paraboloid, the main reflector of modern broadband VGOS radio telescopes is generally designed as a ring-focus paraboloid. According to Cutler (1947), the ring-focus design reduces the fields of decreased intensity caused by shadowing from structural elements, primarily the sub-reflector. For this purpose, the Onsala Twin Telescopes make use of the improved design (Haas *et al* 2019).

According to Lösler *et al* (2017), the canonical expression of an upward-open rotationally symmetric ring-focus paraboloid is defined as

$$\frac{1}{4f}\left((u - rn_u)^2 + (v - rn_v)^2\right) = w, \tag{20}$$

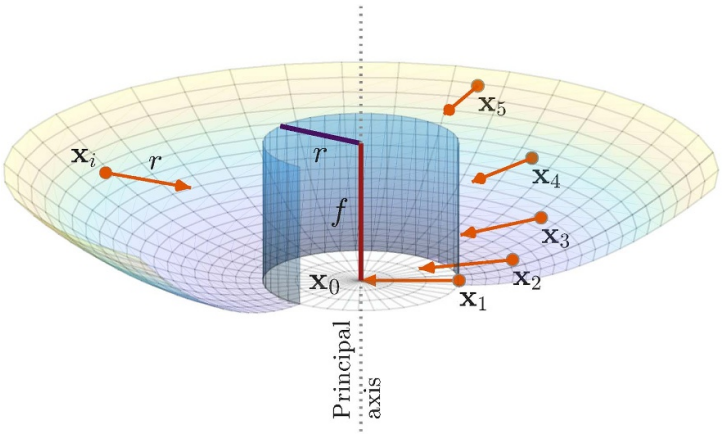

Figure 10. Schematic representation of a sectioned ring-focus paraboloid with focal length f. The imaginary coaxial cylinder with radius r radially displaces the paraboloid's branches at the apex $\mathbf{x}_0$. Some arbitrary distributed surface points $\mathbf{x}_i$ are marked as orange dots, together with the related normal vectors of length r pointing toward the principal axis.

where u, v, w are the coordinates of an arbitrary point lying on the surface. The datum invariant parameters forming the shape are the focal length f and the ring-radius r. The normalized normal vector $\begin{pmatrix} n_u & n_v & 0 \end{pmatrix}^\top$ is perpendicular to both the principal axis of the ring-focus paraboloid and to the surface of the coaxial cylinder with radius r. The vector elements are given by

$$n_u = \frac{u}{\sqrt{u^2 + v^2}}, \tag{21a}$$

$$n_v = \frac{v}{\sqrt{u^2 + v^2}}. \tag{21b}$$

Substituting equations (21) into equation (20) yields the compact expression

$$\frac{1}{4f}\left(\sqrt{u^2 + v^2} - r\right)^2 = w. \tag{22}$$

The rotationally symmetric ring-focus paraboloid degenerates to an ordinary rotationally symmetric paraboloid for $r = 0$. Thus, equation (20) provides a uniform mathematical expression for both main reflector designs (Lösler *et al* 2019, 2022a).

For the general case of a shifted and arbitrarily oriented ring-focus paraboloid, the surface coordinates are derived from a rigid body transformation and substituted into equation (22). Analogously to equation (8), the transformation reads

$$\begin{pmatrix} u \\ v \\ w \end{pmatrix} = \mathbf{R}^\top (\mathbf{x} - \mathbf{x_0}),$$

where the rotation matrix $\mathbf{R}$ defines the orientation and $\mathbf{x}_0$ denotes the apex position of the ring-focus paraboloid.

Figure 10 depicts a schematic representation of a ring-focus paraboloid. The blue indicated cylinder is merely an illustrative geometry and is not a physical component of the main reflector. Hence, only the parabolic surface is actually realized.

7. Results and discussion

The experiments conducted at identical elevation angles were combined at the observation level during the bundle adjustment, thereby defining the datasets for each configuration under investigation. Since the stability of the camera could not be assumed across all experiments, an individual camera model was introduced into the adjustment procedure for each experiment, as proposed by Luhmann *et al* (2023), p353. Thus, the camera was *in-situ* calibrated. According to section 5.2, the stochastic model was defined by the dispersion matrices of the centres of the ellipses derived from the projected circular targets, as well as of the variances of the scales. Positive and negative correlations between the coordinates of the

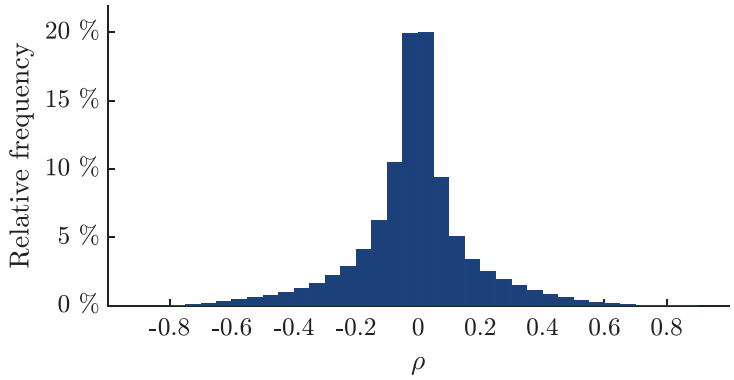

Figure 11. Histogram of mutual correlations ρ between the coordinate components of the ellipse centres derived from the projected circular targets.

centres were almost balanced as indicated in figure 11. Approximately 40% of the correlation coefficients exceeded 10%, with the maximum value being about 80%. Thus, the general assumption of independently and identically distributed image coordinates was not satisfied.

The eccentricity corrections were applied to the image coordinates to minimize the systematic projection errors, as discussed in section 5.3. Due to the small target size relative to the distance from the camera to the main reflector, 99% of the correction terms were $<<0.03$ px. The corrections are smaller than the image blur and therefore have only a marginal impact on the adjustment results. According to Luhmann *et al* (2023), p531, eccentricities less than 0.3 px are negligible in industrial photogrammetry.

According to JCGM100 (2008), p23, mutual correlations have to be taken into account during the data analysis to obtain reliable results. However, most commercial software packages restrict the stochastic model of the bundle adjustment to variances of image coordinates but correlations cannot be specified. Moreover, these software packages typically provide the estimated coordinates along with the corresponding standard deviations but refrain from deriving the fully populated dispersion matrix. Thus, information about existing algebraic correlations between the parameters disappears. This information is often underestimated, particularly in subsequent applications where results of a prior adjustment are treated as input data. However, neglecting correlations affects the derived results and may lead to misinterpretations and incorrect conclusions, as discussed in detail by e.g. Meija and Mester (2008), Lösler *et al* (2021), Kermarrec *et al* (2022), Wu *et al* (2023). In order to consider correlations in stochastic modelling and to obtain the fully populated dispersion matrix, the software package JAiCov (2025) was developed and used to perform the bundle adjustments. The implemented algorithm is described in detail by Lösler *et al* (2022b).

7.1. Impact of long reference scale on bundle adjustment

Key data of the bundle adjustment performed for each configuration under investigation are summarized in table 2. The number of unknown parameters includes the number of surface points and depends on the number of camera models and on the number of images, corresponding to the parameters of the interior and exterior orientations, respectively. The large number of observations relative to the parameters to be estimated indicates high observational redundancy, resulting in a root mean square (*RMS*) error of the surface points of about 50 µm. Such precision is typical for so-called hyper redundant imaging station configurations, as demonstrated by Fraser *et al* (2005).

In order to investigate the impact of a long reference scale on the adjustment results, each configuration was analysed twice, either including or excluding the long scale. Figure 12 compares the resulting correlation coefficients of the 204 surface points for the 40° configuration, including and excluding the long scale. Low correlations are depicted by white or light colours, while stronger positive or negative correlations are shown in red or blue, respectively. Corresponding histograms depict the correlation distributions, where L and S denote the configuration including and excluding the long reference scale, respectively. Obviously, the correlations are larger for the S-configuration, with 68% of the correlation coefficients exhibiting a reduction of at least 50%. Almost the whole range from -1 to $+1$ is covered for the S-configuration. For instance, about 65% of the correlation coefficients exceed 0.2. In contrast, the

Table 2. Summary of bundle adjustment parameters for each configuration including a long reference scale. The elevation angle is denoted by ϵ and *RMS* refers to the root mean square of the surface points.

ϵ	Experiments	Unknowns	Observations	*RMS*
6°	7	14 072	878 579	50 µm
10°	9	17 484	1 071 399	44 µm
20°	10	19 832	1 232 820	53 µm
30°	10	20 156	1 249 354	46 µm
40°	10	21 338	1 274 548	49 µm
50°	10	23 084	1 360 628	48 µm
60°	14	32 980	2 020 992	38 µm
70°	10	23 858	1 425 580	48 µm
80°	10	25 778	1 542 350	47 µm
90°	9	23 175	1 388 291	39 µm

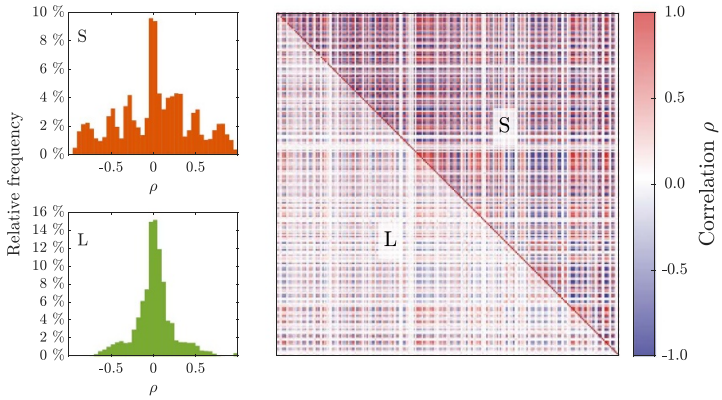

Figure 12. Mutual correlations ρ of the 204 surface points of the ring-focus paraboloid, derived from the fully populated dispersion matrix of the bundle adjustments for the $\epsilon = 40°$ configuration. The orange upper histogram and upper triangular matrix refer to the dataset excluding the long reference scale (labelled S), while the green lower histogram and lower triangular matrix correspond to the dataset including the long scale (labelled L).

L-configuration exhibits a pronounced concentration within ±0.25, and 72% of the correlation coefficients are, for instance, less than 0.2, indicating the strong impact of the long reference scale on the estimates. This pronounced reduction in mutable correlations confirms laboratory experiments conducted by Lösler *et al* (2025c).

Besides the changes in the mutual correlations, the shape of the point-related confidence ellipsoids also depends on the scale definition considered in the bundle adjustment as indicated in figure 13. A point-related confidence ellipsoid corresponds to the 3×3 sub-matrix extracted from the obtained dispersion matrix of the bundle adjustment. The eigenvalues λ of the sub-matrix correspond to the semi-axes of the ellipsoid defining the shape, while the corresponding eigenvectors define the orientation. The orientation can be neglected if the confidence ellipsoid is isotropic and shaped like a sphere (see Grafarend 1985). Thus, the ratio between the minor and major semi-axis given by $\sqrt{\lambda_{\min}}/\sqrt{\lambda_{\max}}$ quantifies the closeness to the ideal isotropic shape. As shown in figure 13, the ratio increases significantly if the long scale is included.

The standard deviations of the coordinate components depend on the chosen datum and are not rotationally invariant (JCGM102 2011, p43). Therefore, they are unsuitable for objective comparisons. However, the ratio $V_{\mathrm{L}}/V_{\mathrm{S}}$ of the volumes of the point-related confidence ellipsoids is rotationally independent and clearly reflects any improvement in precision. The ratio of the mean volumes is 0.5. Including the long reference scale thus halves the confidence regions and underscores the advantage of long reference scales.

7.2. Impact of long reference scale on radio telescope's focal length

The estimated coordinates of the surface points, as well as the corresponding fully populated dispersion matrix, were treated as input data to derive the change in the focal length of the radio telescope for each configuration using equation (20). To account for variations in the focal length in VLBI analysis, knowledge of the relative changes with respect to a reference elevation angle ϵ_0 is sufficient (Clark

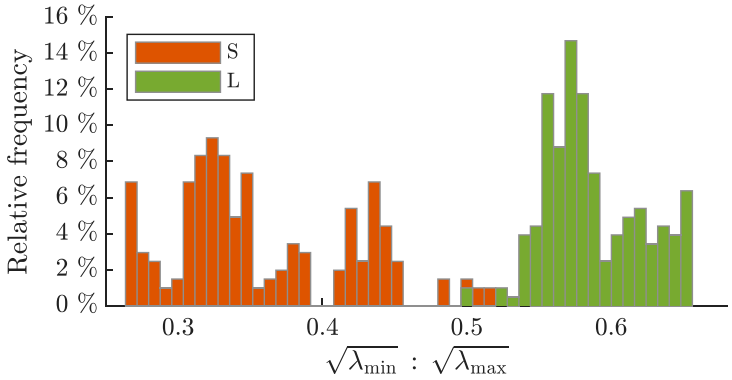

Figure 13. Ratio between the minor and major semi-axis of the confidence ellipsoids of the 204 surface points obtained from the bundle adjustment results excluding (orange, labelled S) and including the long scale (green, labelled L). The results refer to the $\epsilon = 40°$ configuration.

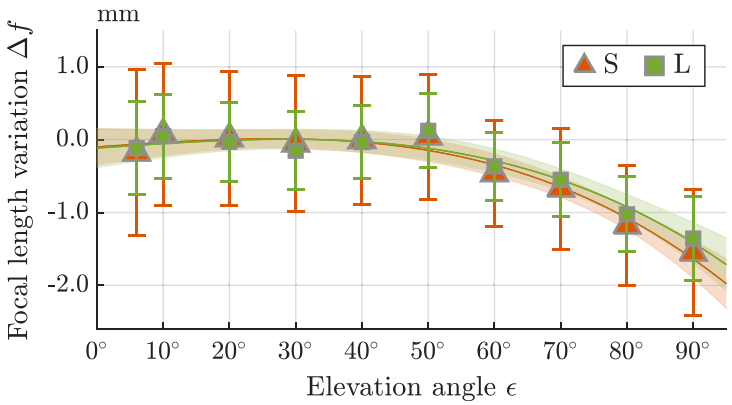

Figure 14. Variation of the focal length w.r.t. $\epsilon_0 = 34°$ derived from the bundle adjustment results excluding (orange, labelled S) and including the long scale (green, labelled L). Error bars and error bands indicate the 99% confidence interval of single measured values and prediction functions, respectively.

Table 3. Estimated coefficients of the derived prediction functions w.r.t. $\epsilon_0 = 34°$ and related standard deviations when excluding (S) and including (L) the long reference scale, respectively.

	p_0	p_1	p_3
S	-0.099 ± 0.096 mm	$6.24 \pm 3.45 \times 10^{-3}$ mm/°	$-2.88 \pm 0.40 \times 10^{-6}$ mm/°^{3}
L	-0.115 ± 0.103 mm	$6.37 \pm 3.69 \times 10^{-3}$ mm/°	$-2.57 \pm 0.43 \times 10^{-6}$ mm/°^{3}

and Thomsen 1988). The panels forming the main reflector shape of the Onsala Twin Telescopes were adjusted by the manufacturer at $\epsilon_0 = 34°$ (Lösler *et al* 2019). Thus, this telescope orientation can serve as a suitable reference.

An adapted polynomial function,

$$p(\epsilon) = p_0 + p_1\epsilon + p_3\epsilon^3, \tag{23}$$

with coefficients p_0, p_1, p_3 was applied to predict the focal length variations of the radio telescope in relation to the elevation angle ϵ. Based on the results of hypothesis testing, the quadratic term was omitted to avoid overparameterization. In order to investigate the impact of a long reference scale in subsequent applications, each configuration was analysed twice, either including or excluding the long scale. Figure 14 depicts the derived variation of the focal length for each configuration. Green values correspond to datasets that include the long reference scale, whereas for the orange values, the long scale was excluded. Prediction functions are plotted in corresponding colours, and the estimated coefficients are summarized in table 3.

Up to about 60°, the focal length of the radio telescope remains highly stable and changes are not detectable. Afterwards, the focal length decreases by up to 1.5 mm, reaching the minimum at 90°. The

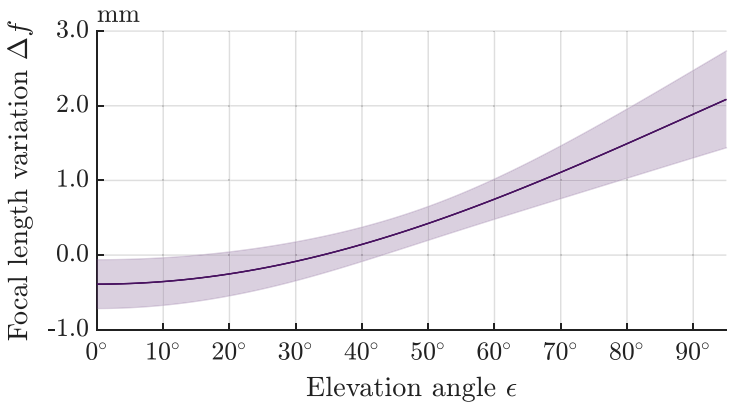

Figure 15. Variation of the focal length w.r.t. $\epsilon_0 = 34°$ derived in 2018 for the northeastern VGOS radio telescope (Lösler *et al* 2019). The error band indicates the 99% confidence interval.

derived prediction functions are almost identical, with the largest deviation of about 0.3 mm at 90°. However, this deviation is covered by the derived dispersion and, thus, is statistically insignificant.

While the estimated parameters remain almost unaffected, the derived uncertainties are mainly influenced by the consideration of a long reference scale. This is expected, since the long reference scale primarily enhances the reliability, as indicated in figures 12 and 13. The mean standard deviations of the estimated focal lengths are 350 µm and 200 µm when excluding and including the long reference scale, respectively. This represents a significant improvement of 40%. Thus, using long reference scales is recommended to improve the reliability and to increase the precision in industrial photogrammetry.

In 2018, the focal length variation of the northeastern VGOS radio telescope at the Onsala Space Observatory was investigated in detail. Figure 15 depicts the prediction function obtained by Lösler *et al* (2019). The focal length varies by about 2 mm. In contrast to the southwestern VGOS radio telescope under investigation, the variation of the northeastern VGOS radio telescope increases with increasing elevation angle.

Even if both radio telescopes are identical in design, the deformation behaviour of both main reflectors differs, emphasizing the need to investigate each radio telescope individually. Transferring the correction between the radio telescopes does not reduce the error but rather exacerbate the problem, and is not recommended.

8. Conclusion

Establishing large physical scales is challenging in industrial environments, particularly when the object under investigation is movable or rotatable, or has to be measured in-process. In this contribution, the gravity-induced deformation behaviour of the main reflector of a modern 13.2 m VLBI radio telescope at the Onsala Space Observatory was investigated by means of industrial close-range photogrammetry, and the benefit of a reference scale exceeding the reflector dimensions was studied in detail. Beside six physical 1.3 m scale bars mounted on the rim of the dish, the supporting struts, and the sub-reflector, a 14.2 m long reference scale was established and its impact on the results was studied. The long scale was realized by two plates installed on the steerable main reflector of the VLBI radio telescope. The main reflector was observed photogrammetrically in different orientations, and dimensional measurements between the plates were performed in-process using two mobile laser trackers. The mean of the derived standard deviation was about 70 µm and only about five times larger than for the short physical scale bars.

The stochastic model for the photogrammetric bundle adjustment was derived from the detected ellipses of the projected circular targets, exploiting the self-similarity between these ellipses and the confidence ellipses of their centres. Including the long reference scale in the bundle adjustment significantly affected the shape of the point-dependent confidence ellipsoids, making them more isotropic and reducing their volume. Moreover, the mutual correlations between the parameters to be estimated were substantially reduced when the long reference scale was considered. However, as almost a complete decorrelation of the data was not achieved, it is strongly recommended to account for the fully populated dispersion matrix in subsequent applications, such as surface fitting or deformation analysis.

The change in the focal length of the VGOS radio telescope was determined with respect to the telescope's elevation angle, and a corresponding prediction function was derived. Including or excluding the long reference scale had only a marginal effect on the derived focal lengths, and almost identical results were obtained. However, introducing the long scale notably reduced the obtained standard deviations. Thus, the reduction in mutual correlations and improved object point uncertainties resulting from the inclusion of the long reference scale in the bundle adjustment were propagated to subsequent applications. Therefore, the use of long reference scales is recommended to improve reliability and precision.

Up to an elevation angle of 60°, the back-end structure of the main reflector responds appropriately to gravity forces, resulting in a stable focal length. For higher elevations, the focal length slightly decreases with increasing elevation angle, reaching the maximum deviation of −1.5 mm at 90°. Comparing the derived focal length changes of both VGOS radio telescopes at Onsala shows similar magnitudes of deviation but different deformation behaviours. Whereas the focal length of the 2018 examined northeastern telescope increases with increasing elevation angle, the focal length of the 2025 investigated southwestern telescope exhibits an opposite trend. Even if both radio telescopes are identical in design, the deformation behaviour differs—a twin is not a clone. For that reason, it is strongly advised to investigate the deformation behaviour of each radio telescope individually.

Acknowledgments

We thank Ansgar Greiwe and Katharina Schulz from University of Applied Sciences Bochum for operating the drone at the Onsala Space Observatory and providing the raw image data. We would also like to show our gratitude to Magnus Kjerling, Jan Karaskuru and Rolf Ahlman from the mechanical workshop at the Onsala Space Observatory for their support in preparing the radio telescope. The T-Scan was kindly provided by Hexagon.

Data availability statement

The photogrammetric datasets analysed during the current study are available in the Zenodo repository, https://doi.org/10.5281/zenodo.17632329.

Funding

This research project received funding from the Erna and Victor Hasselblad Foundation (Gothenburg).

Author contributions

Michael Lösler 0000-0002-1979-263X
Conceptualization (equal), Formal analysis (equal), Investigation (equal), Methodology (equal), Software (equal), Visualization (equal), Writing – original draft (equal), Writing – review & editing (equal)

Kira-Lynn Kopitzke 0009-0008-5567-1641
Formal analysis (equal), Investigation (equal), Software (equal), Writing – review & editing (equal)

Cornelia Eschelbach 0000-0003-4959-8712
Conceptualization (equal), Investigation (equal), Supervision (equal), Writing – review & editing (equal)

Rüdiger Haas 0000-0003-2681-9228
Conceptualization (equal), Funding acquisition (equal), Project administration (equal), Writing – review & editing (equal)

Appendix. Dispersion of ellipse centre

Let x_c', y_c' denote the centre, a_1, a_2 be the semi-axes, and ϕ be the orientation angle of an arbitrarily oriented ellipse expressed by

$$E(x_i,y_i) = \frac{\left(\cos(\phi)\,(x_i - x_c') + \sin(\phi)\,(y_i - y_c')\right)^2}{a_1^2} + \frac{\left(\cos(\phi)\,(y_i - y_c') - \sin(\phi)\,(x_i - x_c')\right)^2}{a_2^2} = 1, \tag{24}$$

where x_i, y_i are the coordinates of a point lying on the curve. The corresponding parametric representation with parameter $t_i \in [0, 2\pi)$ reads

$$E(t_i) = \frac{a_1^2\cos^2(t_i)}{a_1^2} + \frac{a_2^2\sin^2(t_i)}{a_2^2} = 1, \tag{25}$$

and results from the substitution of

$$x_i - x_c' = a_1\cos(\phi)\cos(t_i) - a_2\sin(\phi)\sin(t_i), \tag{26a}$$
$$y_i - y_c' = a_1\sin(\phi)\cos(t_i) + a_2\cos(\phi)\sin(t_i) \tag{26b}$$

into equation (24). Let x_i, y_i be n independent and identically distributed random variables with variance σ_0^2. Without loss of generality, the variance is set to $\sigma_0^2 = 1$, and the dispersion $\mathbf{\Sigma}$ of the ellipse parameters results from

$$\mathbf{\Sigma}^{-1} := \mathbf{N} = \mathbf{A}^\top\mathbf{A}. \tag{27}$$

The Jacobian matrix $\mathbf{A}$ is defined by five column vectors

$$\mathbf{a}_j^\top = \begin{pmatrix} a_{1j} & a_{2j} & \dots & a_{ij} & \dots & a_{nj} \end{pmatrix}$$

corresponding to the ellipse parameters. The elements a_{ij} contain the partial derivatives w.r.t. the parameters of the ellipse and are given by

$$\begin{aligned}
a_{i1} &:= \frac{\partial E}{\partial x_c'} = -\frac{2}{a_1}\cos(\phi)\cos(t_i) + \frac{2}{a_2}\sin(\phi)\sin(t_i)\\
a_{i2} &:= \frac{\partial E}{\partial y_c'} = -\frac{2}{a_1}\sin(\phi)\cos(t_i) - \frac{2}{a_2}\cos(\phi)\sin(t_i)\\
a_{i3} &:= \frac{\partial E}{\partial a_1} = -\frac{2}{a_1}\cos^2(t_i)\\
a_{i4} &:= \frac{\partial E}{\partial a_2} = -\frac{2}{a_2}\sin^2(t_i)\\
a_{i5} &:= \frac{\partial E}{\partial \phi} = \frac{2\left(a_2^2 - a_1^2\right)}{a_1 a_2}\cos(t_i)\sin(t_i).
\end{aligned}$$

According to equation (27), the dot products of the column vectors $\mathbf{a}_k^\top\mathbf{a}_j$ are required, which greatly simplify if t_i is uniformly spaced in $[0, 2\pi)$, because the sums of the sines and cosines of t_i are equal to zero. Hence, the matrix $\mathbf{N}$ becomes block-diagonal, i.e.

$$\mathbf{N} = \begin{bmatrix} \mathbf{N}_{11} & \mathbf{0} \\ \mathbf{0} & \mathbf{N}_{22} \end{bmatrix}. \tag{28}$$

The first block corresponds to the centre of the ellipse and reads

$$\mathbf{N}_{11} = 2n\begin{pmatrix} \frac{\cos^2(\phi)}{a^2} + \frac{\sin^2(\phi)}{b^2} & \frac{\left(b^2-a^2\right)\cos(\phi)\sin(\phi)}{a^2b^2} \\ \frac{\left(b^2-a^2\right)\cos(\phi)\sin(\phi)}{a^2b^2} & \frac{\sin^2(\phi)}{a^2} + \frac{\cos^2(\phi)}{b^2} \end{pmatrix}. \tag{29a}$$

The second block refers to the semi-axes as well as the orientation angle, and appears as block-diagonal matrix defined as

$$\mathbf{N}_{22} = \frac{n}{2}\begin{pmatrix} \frac{3}{a_1^2} & \frac{1}{a_1 a_2} & 0 \\ \frac{1}{a_1 a_2} & \frac{3}{a_2^2} & 0 \\ 0 & 0 & \frac{\left(a_2^2-a_1^2\right)^2}{a_1^2 a_2^2} \end{pmatrix}. \tag{29b}$$

The dispersion matrix of the coordinates of the ellipse centre results from $\boldsymbol{\Sigma}' := \mathbf{N}_{11}^{-1}$. As the determinant $\det(\mathbf{N}_{11}) = \frac{4n^2}{a_1^2 a_2^2} > 0$ is nonzero, the inverse exists and can be expressed explicitly as

$$\begin{aligned}
\boldsymbol{\Sigma}' &= \frac{a_1^2 a_2^2}{2n} \begin{pmatrix} \frac{\sin^2(\phi)}{a^2} + \frac{\cos^2(\phi)}{b^2} & -\frac{\left(b^2-a^2\right)\cos(\phi)\sin(\phi)}{a^2 b^2} \\ -\frac{\left(b^2-a^2\right)\cos(\phi)\sin(\phi)}{a^2 b^2} & \frac{\cos^2(\phi)}{a^2} + \frac{\sin^2(\phi)}{b^2} \end{pmatrix} \\
&= \frac{1}{2n} \begin{pmatrix} a_1^2\cos^2(\phi) + a_2^2\sin^2(\phi) & a_1^2\cos(\phi)\sin(\phi) - a_2^2\cos(\phi)\sin(\phi) \\ a_1^2\cos(\phi)\sin(\phi) - a_2^2\cos(\phi)\sin(\phi) & a_1^2\sin^2(\phi) + a_2^2\cos^2(\phi) \end{pmatrix} \\
&= \frac{1}{2n} \begin{pmatrix} \cos(\phi) & -\sin(\phi) \\ \sin(\phi) & \cos(\phi) \end{pmatrix} \begin{pmatrix} a_1^2 & 0 \\ 0 & a_2^2 \end{pmatrix} \begin{pmatrix} \cos(\phi) & \sin(\phi) \\ -\sin(\phi) & \cos(\phi) \end{pmatrix} \\
&= \mathbf{R}_\phi \boldsymbol{\Lambda} \mathbf{R}_\phi^\top . \qquad (30)
\end{aligned}$$

The orthogonal matrix $\mathbf{R}_\phi$ contains the eigenvectors and defines the orientation of the confidence ellipse through the angle ϕ. The corresponding eigenvalues, which determine the shape of the ellipse, are given by $\boldsymbol{\Lambda}$. These eigenvalues correspond to the (scaled) semi-axes a_1 and a_2. Thus, the confidence ellipse of the centre is self-similar to the original ellipse.

References

Ahn S J, Warnecke H-J and Kotowski R 1999 Systematic geometric image measurement errors of circular object targets: mathematical formulation and correction *Photogramm. Rec.* **16** 485–502

Bergstrand S, Herbertsson M, Rieck C, Spetz J, Svantesson C-G and Haas R 2019 A gravitational telescope deformation model for geodetic VLBI *J. Geod.* **93** 669–80

Canny J 1986 A computational approach to edge detection *IEEE Trans. Pattern Anal. Mach. Intell.* **PAMI-8** 679–98

Clark T A and Thomsen P 1988 Deformations in VLBI antennas *Technical Report* NASA-TM-100696 NASA, NASA Goddard Space Flight Center Greenbelt, MD, United States

Cutler C C 1947 Parabolic-antenna design for microwaves *Proc. IRE* **35** 1284–94

Deriche R 1987 Using Canny's criteria to derive a recursively implemented optimal edge detector *Int. J. Comput. Vis.* **1** 167–87

Dold J 1996 Influence of Target Size on the Results of Photogrammetric Bundle Adjustment *Xviiith Isprs Congress – Technical Commission V: Close Range Techniques and Machine Vision* vol XXXI, B5 (International Archives of Photogrammetry and Remote Sensing) pp 119–23

Dold J 1997 Ein hybrides photogrammetrisches Industriemeßsystem höchster Genauigkeit und seine Überprüfung Hochschule der Bundeswehr München, Fachbereich Bauingenieur- und Vermessungswesen

Fraser C S, Woods A and Brizzi D 2005 Hyper redundancy for accuracy enhancement in automated close range photogrammetry *Photogramm. Rec.* **20** 205–17

Fu L-B, Liu J-J, Yan W, Kong D-Q, Ren X, Liu C-D and Zhang H-B 2022 Gravitational deformation measurement method for the main reflector and sub-reflector of the 70 m antenna by laser scanner *Res. Astron. Astrophys.* **22** 095001

Godding R 2017 Camera Calibration *Handbook of Machine and Computer Vision – The Guide for Developers and Users* 2nd edn (Wiley) pp 291–316

Grafarend E W 1985 Criterion Matrices for Deforming Networks *Optimization and Design of Geodetic Networks* (Springer) pp 363–428

Granshaw S I 1980 Bundle adjustment methods in engineering photogrammetry *Photogramm. Rec.* **10** 181–207

Grün A 1982 The accuracy potential of the modern bundle block adjustment in aerial photogrammetry *Photogramm. Eng. Remote Sens.* **48** 45–54

Haas R *et al* 2019 Status of the Onsala twin telescopes – two years after the inauguration *Proc. 24th European VLBI for Geodesy and Astrometry (EVGA) Working Meeting* pp 5–9

Hexagon 2012 *Leica Absolute Tracker AT401 – Absolutely Portable –* (*Product Brochure*)

Hexagon 2015a *Leica Absolute Tracker AT960 – Absolute Portability, Absolute Speed, Absolute Accuracy –* (*Product Brochure*)

Hexagon 2015b *Leica T-Scan 5 – The Most Dynamic Laser Scanner Ever –* (*Product Brochure*)

Hexagon 2021 *Formulas for Refraction Indices Used in the Leica Absolute Tracker AT40x, AT9x0 and ATS600, Laser Tracker Products – Technical Documents*

Holst C, Schunck D, Nothnagel A G, Haas R, Wennerbäck L, Olofsson H, Hammargren R and Kuhlmann H 2017 Terrestrial laser scanner two-face measurements for analyzing the elevation-dependent deformation of the onsala space observatory 20-m radio telescope's main reflector in a bundle adjustment *Sensors* **17** 1–21

IVS 2019 *Surveys of Radio Telescopes for Modeling of Gravitational Deformation* (available at: https://ivscc.gsfc.nasa.gov/about/resolutions/IVS-Res-2019-01-TelescopeSurveys.pdf)

JAG3D 2025 JavaAppliedGeodesy3D—least-squares adjustment software for geodetic sciences (https://doi.org/10.5281/zenodo.7424594)

JAiCov 2025 Java Aicon covariance matrix—bundle adjustment for close-range photogrammetry (available at: https://github.com/applied-geodesy/bundle-adjustment)

JCGM100 2008 *Evaluation of measurement data—guide to the expression of uncertainty in measurement—GUM 1995 with minor corrections* Bureau International des Poids et Mesures (BIPM) (https://doi.org/10.59161/JCGM100-2008E)

JCGM102 2011 *Evaluation of measurement data—Supplement 2 to the'Guide to the expression of uncertainty in measurement'—extension to any number of output quantities* Bureau International des Poids et Mesures (BIPM) (https://doi.org/10.59161/JCGM102-2011)

Kahmen O and Luhmann T 2016 Entwicklung einer großen Invardraht-Maßverkörperung zur Anwendung in der Industriephotogrammetrie *Dreiländertagung der SGPF, DGPF und OVG, Lösungen für eine Welt im Wandel,* 25 (*Bern*)*36th Wissenschaftlich-Technische Jahrestagung der DGPF* pp 538–44 (Publikationender Deutschen Gesellschaft für Photogrammetrie, Fernerkundung und Geoinformation e.V. (DGPF))

Kermarrec G, Lösler M, Guerrier S and Schön S 2022 The variance inflation factor to account for correlations in likelihood ratio tests: deformation analysis with terrestrial laser scanners *J. Geod.* **96** 86
Koch K-R 1985 First Order Design *Optimization and Design of Geodetic Networks* (Springer) pp 56–73
Kopitzke K-L 2026 Prozessbegleitende Referenzlängenbestimmung von großen drehbaren Objekten in photogrammetrischen Anwendungen *VDVmagazin* **77** 122–30
Lehmann R and Lösler M 2026 Symmetric versus non-symmetric least squares solution for spatial coordinate transformations *Proc. 2026 IAG Scientific Assembly, Int. Association of Geodesy Symp. Reference Frames for Applications in Geosciences (REFAG)* (Springer) pp 1–7
Liebold F and Maas H-G 2024 Eccentricity correction methods for circular targets in perspective projection *Int. Arch. Photogramm. Remote Sens. Spatial Inf. Sci.* **XLVIII-2/W7-2024** 65–72
Lösler M, Kopitzke K-L, Eschelbach C, Greiwe A and Schulz K 2026 Dataset for Considering a Long Reference Scale in Photogrammetric Bundle Adjustment for Evaluating Gravity-Induced Focal Length Variation of a VGOS Radio Telescope *Zenodo* (https://doi.org/10.5281/zenodo.17632329)
Lösler M, Eschelbach C, Greiwe A, Brechtken R, Plötz C, Kronschnabl G and Neidhardt A 2022a Ray tracing-based delay model for compensating gravitational deformations of VLBI radio telescopes *J. Geodetic Sci.* **12** 165–84
Lösler M, Eschelbach C, Greiwe A, Zhou B and McCallum L 2025a Innovative approach for modelling gravity-induced signal path variations of VLBI radio telescopes *Earth Planets Space* **77** 9
Lösler M, Eschelbach C and Haas R 2017 Unified model for surface fitting of radio telescope reflectors *Proc. 23rd European VLBI for Geodesy and Astrometry (EVGA) Working Meeting* pp 29–34
Lösler M, Eschelbach C and Haas R 2025b Pointing-dependent variation of a radio telescope reference point – first investigation at the Onsala Space Observatory *zfv* **150** 319–27
Lösler M, Eschelbach C and Klügel T 2022b Close range photogrammetry for high-precision reference point determination: a proof of concept at satellite observing system Wettzell *Proc. 2021 IAG Scientific Assembly, Int. Association of Geodesy Symposia* vol 154 *Geodesy for a Sustainable Earth* (Springer) pp 57–65
Lösler M, Eschelbach C, Klügel T and Riepl S 2021 ILRS reference point determination using close range photogrammetry *Appl. Sci.* **11** 2785
Lösler M, Eschelbach C and Lehmann R 2025c Impact of mathematical correlations: exemplified in industrial applications *J. Appl. Geodesy* **19** 365–75
Lösler M, Haas R, Eschelbach C and Greiwe A 2019 Gravitational deformation of ring-focus antennas for VGOS—first investigations at the Onsala twin telescopes project *J. Geod.* **93** 2069–87
Lösler M, Kopitzke K-L and Eschelbach C 2026 On the suitability of spherical glass-body reflectors in industrial applications *Proc. 21th Int. Course on Engineering Surveying 2026* (Verlag der Technischen Universität Graz) pp 158–69
Luhmann T, Robson S, Kyle S and Boehm J 2023 *Close-Range Photogrammetry and 3D Imaging* 4th edn (Walter de Gruyter GmbH)
Martin O C, Robson S, Kayani A, Muelaner J E, Dhokia V and Maropoulos P G 2016 Comparative performance between two photogrammetric systems and a reference laser tracker network for large-volume industrial measurement *Photogramm. Rec.* **31** 348–60
Meija J and Mester Z 2008 Uncertainty propagation of atomic weight measurement results *Metrologia* **45** 53–62
MSR 2024 *MSR 145: Mini Data Logger for Temperature, Humidity, Pressure, Light, Acceleration*
Nothnagel A G 2025 Radio telescope dimensions for geodetic and astrometric VLBI thermal expansion modelling *TU Wien* (https://doi.org/10.48436/W41MS-22Q67)
Nothnagel A G, Holst C and Haas R 2019 A VLBI delay model for gravitational deformations of the Onsala 20 m radio telescope and the impact on its global coordinates *J. Geod.* **93** 2019–36
Otepka J O and Fraser C S 2004 Accuracy enhancement of vision metrology through automatic target plane determination *Int. Arch. Photogramm. Remote Sens. Spatial Inf. Sci.* **35** 873–9 (available at: www.isprs.org/proceedings/xxxv/congress/comm5/papers/672.pdf)
Pauli W 1969 Vorteile eines kippbaren Reflektors bei der elektrooptischen Streckenmessung *Vermessungstechnik* **17** 412–5
Pfaffinger T, Nothnagel A and Holst C 2026 Workflow for monitoring gravitational focal length changes of the HartRAO 26 m radio telescope's main reflector *FIG Congress 2026: The Future We Want – The SDGs and Beyond* vol XXVIII (available at: www.fig.net/resources/proceedings/fig_proceedings/fig2026/papers/ts01g/TS01G_pfaffinger_nothnagel_et_al_13712.pdf)
Reznicek J, Ekkel T, Hastedt H, Luhmann T, Kahmen O and Jepping C 2016 Zum Einfluss von Maßstäben in photogrammetrischen Projekten großer Volumina *Photogrammetrie – Laserscanning – Optische 3D-Messtechnik* (Wichmann) Beiträge der 16. Oldenburger 3D-Tage 2016, pp 286–95
Rüeger J M 1978 Misalignment of EDM reflectors and its effects *Aust. Surv.* **29** 28–36
Rüeger J M 1996 *Electronic Distance Measurement – An Introduction* 4th edn (Springer)
Safaee-Rad R, Tchoukanov I, Smith K C and Benhabib B 1992 Three-dimensional location estimation of circular features for machine vision *IEEE Trans. Robot. Autom.* **8** 624–40
Sarti P, Negusini M and Abbondanza C 2011 Improved geodetic European very-long-baseline interferometry solution using models of antenna gravitational deformation *Ann. Geophys.* **53** 13–23
Schuh H and Behrend D 2012 VLBI: a fascinating technique for geodesy and astrometry *J. Geodyn.* **61** 68–80
Varenius E, Haas R and Nilsson T 2021 Short-baseline interferometry local-tie experiments at the Onsala Space Observatory *J. Geod.* **95** 54
Wu E *et al* 2024 Research on fusion and deformation analysis of decade' HLS-II control network surveying data *J. Instrum.* **19** 05043
Wu E, Zhang Q, Wang X, Lin Y, Wang W, Ding T, Ma H and He X 2025 Significance analysis of scale factor in coordinate transformation under multi-condition simulation *J. Instrum.* **20** T09009
Wu Z, Huang B, Fan J and Chen H 2023 Homotopy based stochastic finite element model updating with correlated static measurement data *Measurement* **210** 112512
Xie Y and Ji Q 2002 A new efficient ellipse detection method *Object Recognit. Support. User Interact. Serv. Robots (ICPR-02)* **2** 957–60
Yu L, Chen F, Huang J and Wei X 2015 An ellipse detection algorithm based on edge classification *MIPPR 2015: Autom. Target Recognit. Navig.* **9812** 981209